A&A 509, A50 (2010)
DOI: 10.1051/0004-6361/200912877

Astronomy & Astrophysics

The structure of hot molecular cores over 1000 AU*

R. Cesaroni[1], P. Hofner[2,3,4], E. Araya[5,3,6], and S. Kurtz[7]

[1] Osservatorio Astrofisico di Arcetri, INAF, Largo E. Fermi 5, 50125 Firenze, Italy
e-mail: cesa@arcetri.astro.it
[2] Physics Department, New Mexico Tech, 801 Leroy Place, Socorro, NM 87801, USA
e-mail: phofner@nrao.edu
[3] National Radio Astronomy Observatory, PO Box O, Socorro, NM 87801, USA
[4] Max-Planck-Institut für Radioastronomie, Auf dem Hügel 69, 53913 Bonn, Germany
[5] NRAO Jansky Fellow, Department of Physics and Astronomy, MSC07 4220, University of New Mexico, Albuquerque, NM 87131, USA
e-mail: earaya@nrao.edu
[6] Physics Department, Western Illinois University, 1 University Circle, Macomb, IL 61455, USA
[7] Centro de Radioastronomía y Astrofísica, Universidad Nacional Autónoma de México, Apdo. Postal 3-72, 58089 Morelia, Michoacán, Mexico
e-mail: s.kurtz@crya.unam.mx

Received 13 July 2009 / Accepted 19 October 2009

ABSTRACT

Context. Hot molecular cores (HMCs) are believed to be the cradles of stars of mass above ~6 $M_\odot$. It is hence important to determine their structure and kinematics and thus study phenomena directly related to the star-formation process, such as outflow, infall, and rotation. Establishing the presence of embedded early-type (proto)stars is also crucial for understanding the nature of HMCs.

Aims. To achieve the highest available angular resolution to date, we performed observations of the molecular gas in two well-known HMCs (G10.47+0.03 and G31.41+0.31) with an angular resolution of ~0.″1. Continuum observations were also made at different wavelengths to detect HII regions associated with early-type stars embedded in the cores.

Methods. We used the Very Large Array in its most extended configuration to image the NH_3(4,4) inversion transition. Continuum measurements were made at 7 mm, 1.3 cm, and 3.6 cm using the A-array configuration.

Results. We detected two new continuum sources in G31.41+0.31, which are possibly thermal jets, and confirmed the presence of one ultracompact and two hypercompact HII regions in G10.47+0.03. Evidence that the gas is infalling towards the embedded (proto)stars is provided for both G10.47+0.03 and G31.41+0.31, while in G10.47+0.03 part of the ammonia gas also appears to be expanding in two collimated bipolar outflows. From the temperature profile in the cores, we establish an approximate bolometric luminosity for both sources in the range 1×10^5–7×10^5 $L_\odot$. Finally, a clear velocity gradient across the core is detected in G31.41+0.31. The nature of this gradient is discussed and two alternative explanations are proposed: outflow and rotation.

Conclusions. We propose a scenario where G10.47+0.03 is in a more advanced evolutionary stage than G31.41+0.31. In this scenario, thermal jets develop until the accretion rate is sufficiently high to trap or even quench any HII region. When the jets have pierced the core and the stellar mass has grown sufficiently, hypercompact HII regions appear and the destruction of the HMC begins.

Key words. stars: formation – HII regions – ISM: individual objects: G10.47+0.03, G31.41+0.31 – ISM: molecules

1. Introduction

Understanding the formation mechanism of early-type stars requires knowledge of the environment in which these stars are born. On the basis of the previous studies performed, it is commonly accepted that the so-called "hot molecular cores" (HMCs) are the cradle of high-mass (>6 $M_\odot$) stars. These are dense, compact, dusty cores with temperatures in excess of ~100 K, often found in association with typical signposts of high-mass star formation such as masers, luminous infra-red (IR) sources, or ultracompact (UC) HII regions (see Kurtz et al. 2000 and Cesaroni 2005 for reviews on this topic). While only a limited number of HMCs have been identified to date, the interest in them has grown because they represent ideal laboratories for testing theories describing the formation of OB stars. For this purpose, it is crucial to know the detailed structure and velocity field inside HMCs and to estimate their lifetime.

The latter goal can be achieved by determining their relative number with respect to other objects, such as UC HII regions (Wilner et al. 2001; Furuya et al. 2005), but this requires unbiased observations of large regions at high angular resolution to ensure that the results are statistically reliable, a task that is beyond the capabilities of current interferometers. The advent of ALMA is bound to boost this type of research and dramatically increase the number of known HMCs.

As for the HMC structure, the angular and spectral resolution currently attainable with centimeter and (sub)millimeter interferometry, albeit limited in comparison to future instruments, suffice to investigate the morphology and kinematics of HMCs. Sensitivity is obviously an issue that ALMA will address. Nevertheless, using suitable high temperature tracers one can already partially circumvent this problem and detect

* Based on observations carried out with the NRAO Very Large Array. The National Radio Astronomy Observatory is operated by Associated Universities, Inc., under cooperative agreement with the National Science Foundation.

line emission even at sub-arcsec resolution. A large number of studies have demonstrated the feasibility of these observations, shedding light on the nature of these objects and uncovering phenomena such as rotation and/or infall that have important implications for our knowledge of high-mass star formation (see Cesaroni et al. 2007; Hoare et al. 2007; Beuther et al. 2007).

One consideration is that the typical size of a HMC is ~0.05 pc, while its distance is in most cases >5 kpc, implying an angular diameter <2″. Until recently, (sub)mm interferometers have hardly been able to achieve angular resolutions below 1″, which are sufficient only to barely resolve a HMC. Notwithstanding the improvements achieved by the upgrade of some instruments and observation at shorter (sub-mm) wavelengths, the highest resolution attainable with a connected radio interferometer remains that provided at 1.3 cm and 7 mm by the Very Large Array (VLA) in its most extended configuration.

With this in mind, we have performed observations of two well-known HMCs with the VLA in the continuum and ammonia emission, with the twofold purpose to image the free-free emission from deeply embedded OB stars and to analyse the dense molecular gas enshrouding them. The sources are G10.47+0.03 (hereafter G10) and G31.41+0.31 (hereafter G31), located at distances of 10.8 kpc (Pandian et al. 2008; Sewilo et al. 2004) and 7.9 kpc (Churchwell et al. 1990), respectively. These had been imaged by us in the NH_3(4,4) line using the D, C, and B array configurations (Cesaroni et al. 1994a, hereafter Paper I; Cesaroni et al. 1998, hereafter Paper II). Both objects consist of a HMC plus one or more HII regions classified as ultracompact by Wood & Churchwell (1989). The main morphological difference between G10 and G31 is that in G10 the UC HII regions are embedded in the HMC, whereas in G31 the UC HII region appears to be offset from the core by ~5″. In our studies, besides obtaining estimates of global quantities[1] such as the core mass, we could also barely resolve the HMCs and study the dependence of temperature and column density as functions of the core radius. In particular, we came to the conclusion that the temperature increases outside-in quite steeply, possibly reaching values as high as 400 K close to the centre. The analysis of the line velocity suggested that (part of) the NH_3(4,4) gas in G10 is expanding, while a NE–SW velocity gradient detected in G31 was interpreted as rotation. Based on the temperature profiles and core dynamics, we suggested that HMCs without embedded UC HII regions are likely to harbour younger high-mass (proto)stellar objects.

While our previous observations have permitted us to estimate the physical parameters of the two cores, they did not directly establish the distribution of these parameters in relationship to the embedded objects, because of their insufficient angular resolution. The continuum sensitivity was also insufficiently high to detect any putative young stellar objects (YSO) embedded in G31. In this article, we present A-array observations of the NH_3(4,4) line towards G10 and G31 and new deep continuum images at different frequencies, to circumvent the limitations of our previous studies.

After giving the technical details of the observations in Sect. 2, in Sect. 3 we report on the results obtained, while the derivation of physical quantities and the discussion are presented in Sect. 4. Finally, we draw our conclusions in Sect. 5.

[1] Note that in Papers I and II a distance of 5.8 kpc was adopted for G10.

Table 1. Parameters of VLA observations.

Source	λ (cm)	rms (μJy/beam)	Synth. beam, PA
G10.47+0.03	6.0	269	0.″73 × 0.″42, −11.°2
	3.6	73	0.″37 × 0.″19, −15.°5
	2.0	773	0.″74 × 0.″39, −16.°2
	1.3	227	0.″15 × 0.″092, 6.°8
	NH_3(4,4)	740[a]	0.″15 × 0.″092, 6.°8
G31.41+0.31	3.6	41	0.″24 × 0.″20, 32.°1
	1.3	31	0.″095 × 0.″084, −0.°3
	0.7	85	0.″064 × 0.″047, −15.°1
	NH_3(4,4)	403[a]	0.″11 × 0.″09, −6.°1

[a] In a 2.43 km s^{-1}-wide channel.

2. Observations and data reduction

In this section, we provide technical details of the observations and data reduction. We adopted LSR velocities of 67.3 km s^{-1} for G10 and 97.4 km s^{-1} for G31. All observations were carried out with the VLA, and the calibration and data reduction were made with the NRAO software package AIPS. The relevant observational parameters of the resulting maps are summarised in Table 1.

2.1. Continuum

2.1.1. G10.47+0.03

C-Band – 6 cm: *C*-band continuum data observed with the VLA in the A-configuration in the period March 24–26, 1990 were obtained from the VLA archive (program code AH398). The data were calibrated in the standard way, and the 6 cm map shown in Fig. 1 was made with AIPS task IMAGR using natural weighting. To de-emphasize unrelated extended emission in the area, and to obtain a synthesised beam similar to that of the 1.3 cm B-configuration (Paper II), we restricted the (u, v) data to projected baselines >40 kλ.

X-Band – 3.6 cm: the observations were carried out in the standard continuum mode (i.e., 4IF mode, 50 MHz bandwidth per IF) with the VLA in the A-configuration on November 3, 2000 for a total onsource time of 45 min. The phase centre in B1950 coordinates was RA = $18^h05^m40.30^s$, Dec = −19°52′20.0″ (corresponding to J2000 coordinates RA = $18^h08^m38.22^s$, Dec = −19°51′48.7″). Calibration of the flux density scale was based on observations of 3C 286. Gain amplitude and phase corrections were derived from observations of B1817–254. Two iterations of self-calibration were carried out, which improved the quality of the image slightly. In Fig. 1, we show our ROBUST 0 weighted map.

U-Band – 2 cm: *U*-band continuum data observed in the B-configuration on March 24, 2001, were obtained from the VLA archive (AH726). Standard AIPS calibration procedures were applied. In Fig. 1, we show a ROBUST 0 weighted map using only (u, v) data with projected baseline separations greater than 30 kλ.

K-Band – 1.3 cm: the *K*-band continuum map was derived from averaging all line-free channels of the NH_3 observations described below. In Fig. 1, we show our natural weighted map.

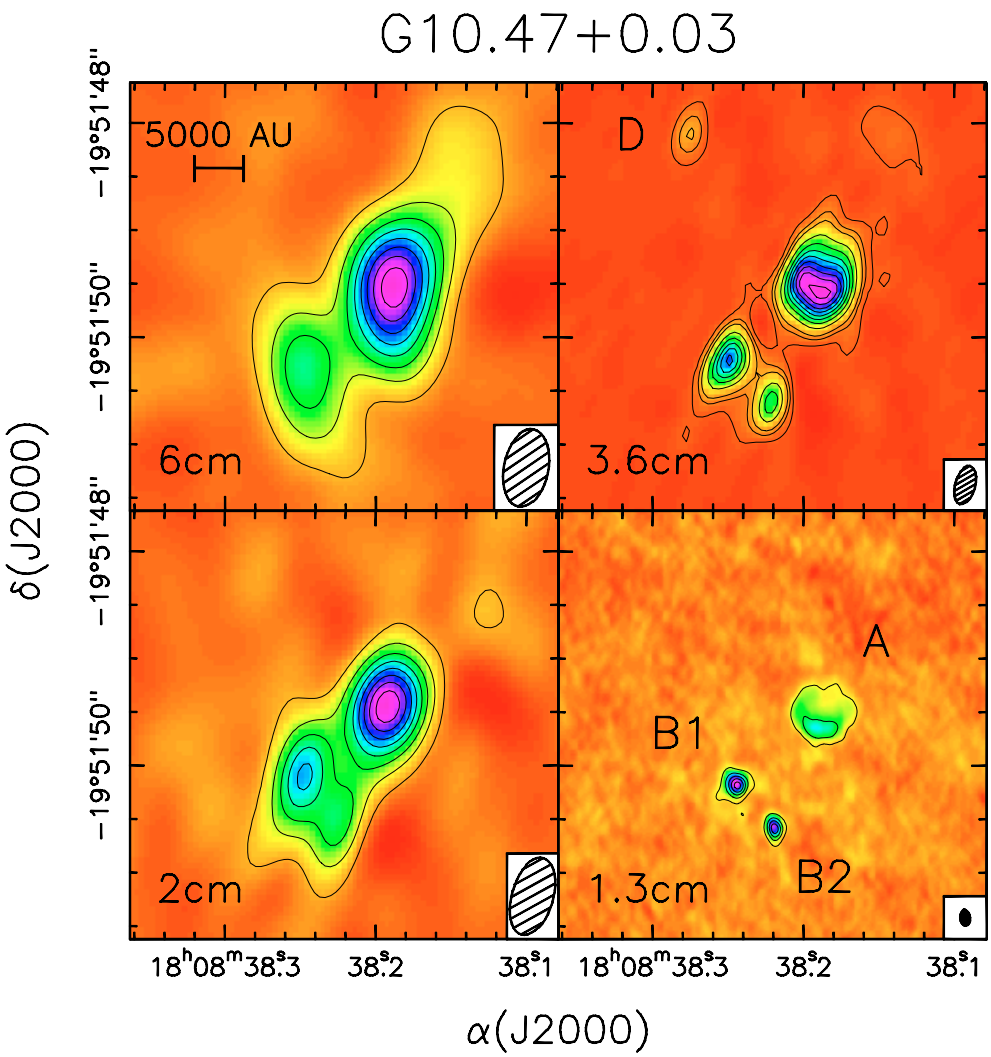

Fig. 1. Images of the continuum emission towards G10.47+0.03. In the *bottom left* of each panel, the observing wavelength is indicated. Letters A, B1, B2, and D denote the different sources detected in the region. Contour levels range from 1.1 to 14.96 in steps of 1.98 mJy/beam at 6 cm, from 0.3 to 1.5 in steps of 0.6 mJy/beam and from 3.3 to 15.9 in steps of 1.8 mJy/beam at 3.6 cm, from 3.45 to 46.92 in steps of 6.21 mJy/beam at 2 cm, and from 1.25 to 10.25 in steps of 2.25 mJy/beam at 1.3 cm.

2.1.2. G31.41+0.31

X-Band – 3.6 cm: we observed the G31.41+0.31 region with the VLA in the A configuration on November 3, 2000 for a total onsource time of about 53 min, using the standard continuum mode. The phase centre in B1950 coordinates was RA = $18^{h}44^{m}59.00^{s}$, Dec = $-01°16'00.0''$ (corresponding to J2000 coordinates RA = $18^{h}47^{m}34.20^{s}$, Dec = $-01°12'39.0''$). Calibration of the flux density scale was based on observations of 3C 286. Gain amplitude and phase corrections were derived every 5 min from observations of B1849+005 and after interpolation applied to the G31.41+0.31 data. The data were converted to the J2000 coordinate system. We estimate that the accuracy of the B1950–J2000 conversion is ~50 mas. To suppress the effects of the strong extended emission in the region, the (u, v) range was restricted to >200 kλ. In Fig. 2 (lower panel), we show our ROBUST 0 weighted map.

K-Band – 1.3 cm: the *K*-band continuum mode observations were carried out on June 11, 2003, with the VLA in the A configuration. We observed 3C 286 and J1851+005 as primary (flux) and secondary (amplitude and phase) calibrators, respectively. The observation method was fast switching with a cycle of 50/30 s (source/calibrator). For flux calibration, we used the *K*-band model of the brightness distribution of 3C 286 provided by NRAO. In Fig. 2 (upper panel), we show our ROBUST 0 weighted map.

Q-Band – 0.7 cm: the VLA *Q*-band continuum observations were conducted on June 5 and 24, 2003. The VLA was in the A-configuration. On both days, 3C 286 was used as a primary (flux) calibrator and J1851+005 as an amplitude and a phase calibrator. We observed using a 30/30 s fast-switching cycle. For flux calibration we used the *Q*-band clean model for 3C 286 provided by NRAO. For J1851+005, we measured a flux of 0.71 Jy and 0.64 Jy on June 5 and June 24, respectively. The variation in the flux density between the two days could be due to the intrinsic variability of the quasar, and/or calibration errors. Assuming that the difference is caused completely by calibration errors, then the flux density calibration would be accurate to within ~10%. In Fig. 2 (both panels), we show our ROBUST 5 weighted map.

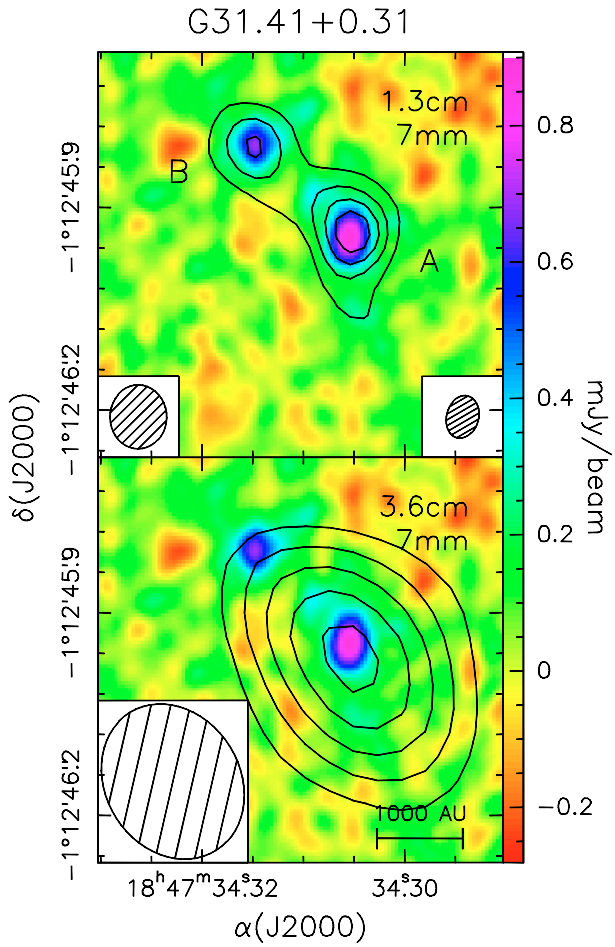

Fig. 2. *Top*: overlay of the 1.3 cm continuum map (contours) on the image of the 7 mm continuum emission (colour scale). The contour levels range from 0.126 to 0.432 in steps of 0.102 mJy/beam. The ellipses to the *bottom left and right* represent the synthesised beams at 1.3 cm and 7 mm, respectively. *Bottom*: same as top, where the 1.3 cm emission is replaced by that at 3.6 cm. The contour levels range from 0.033 to 0.297 in steps of 0.066 mJy/beam. The ellipse represents the synthesised beam at 3.6 cm.

2.2. NH_3(4,4) line

2.2.1. G10.47+0.03

Observations of the NH_3(4,4) transition at 24 139.4169 MHz (Poynter & Kakar 1975) were obtained on November 12 and 18, 2004 with the VLA in the A-configuration. The pointing position was RA = $18^h05^m40.30^s$, Dec = $-19°52'20.0''$ in the B1950 coordinate system (corresponding to J2000 coordinates RA = $18^h08^m38.22^s$, Dec = $-19°51'48.7''$). We used the 1A correlator mode (i.e., right-hand circular polarization only) with a bandwidth of 12.5 MHz and 64 channels of width 195 kHz. This provides a total velocity coverage of about 155 km s^{-1} and a spectral resolution of 2.43 km s^{-1}. Flux density calibration was based on the standard VLA calibrator 3C 286. To derive amplitude and phase calibration, we alternated observations of G10.47+0.03 with the calibrator source B1752−225 on a 50/40 s source-calibrator cycle. Pointing corrections were derived from *X*-band observations of nearby QSO's and applied online. Bandpass corrections were derived from observations of B1730–130 and applied during the calibration. We used the standard data reduction procedure for high frequency data. Data acquired on different days were reduced separately and checked for consistency before being combined. A continuum data set was formed by averaging all line-free channels. The line-only data set was formed by subtracting the continuum data in the (u, v) domain.

2.2.2. G31.41+0.31

The NH_3(4,4) observations were carried out on October 15, 23 and November 5, 2004 with the VLA in the A-configuration. The pointing position was RA = $18^h47^m34.5066^s$, Dec = $-01°12'42.971''$ in the J2000 coordinate system. The spectral line setup was identical to the G10.47+0.03 line observations described above. To derive amplitude and phase calibration, we alternated observations of G31.41+0.31 with the calibrator source J1851+005 on a 80/40 s source-calibrator cycle. Pointing, bandpass calibration (from observations of J1733–130), continuum subtraction, and imaging were the same as for G10.

3. Results

3.1. Continuum

Figure 1 shows the continuum maps of G10. These confirm the existence of three HII regions inside the HMC, one of which (G10 A) is clearly resolved in our new 3.6 cm and 1.3 cm A-array images and has a cometary shape. This shape is consistent with the UC HII region being closer to the HMC surface, as discussed in Paper II. In this case, the HII region must be density bounded towards the HMC centre, whereas in the opposite direction the ionised gas expands forming a "tail", because of the lower confinement provided by the lower density gas surrounding the HMC.

The main parameters of the three HII regions are given in Table 2, for each object and observing wavelength: the peak position in equatorial coordinates; the peak flux, $F_{\rm peak}$; the corresponding brightness temperature measured in the synthesised beam, $T_{\rm SB}$; the full width at half power, *FWHP*; the deconvolved angular diameter, $\Theta_{\rm S}$ (assuming a Gaussian shape for both the beam and the source); the flux density integrated over the source, S_ν; and the 1σ rms noise of the image. The *FWHP* was measured to be as the diameter of the circle whose area equals that enclosed by the 50% contour level, i.e., $FWHP = 2\sqrt{A/\pi}$, while the deconvolved diameter is given by the expression $\Theta_{\rm S} = \sqrt{FWHP^2 - HPBW^2}$, where *HPBW* is the half power width of the synthesised beam, and S_ν is calculated by integrating the emission inside the 5σ contour level.

One can see that, unlike G10 A, the other two HII regions are almost unresolved at 1.3 cm. This finding appears to contradict the results obtained in Paper II after merging the D, C, and B configurations. From their Table 3, one can see that the deconvolved source diameter of these two objects is much larger than the synthesised beam of our A-array observations. This can be explained if the brightness profile of the HII region resembles a power law. We comment further on this issue in Sect. 4.1.1. Because of their small size, in the following we refer to B1 and B2 as hypercompact (HC) HII regions, whilst A is called UC HII region.

A final consideration about Fig. 1 is the presence of a previously unknown source to the north that we name G10 D. This is only barely resolved with a deconvolved diameter of ~0.″12 (see Table 2) and detected only at 3.6 cm with a flux density of 1.7 mJy, so that it is not possible to establish its nature from the spectral energy distribution. Based on the assumption that it is an optically thin HII region, from the 3.6 cm flux density

Table 2. Observed parameters of the continuum sources in G10.47+0.03.

Source	λ (cm)	α(J2000)	δ(J2000)	$F_{\rm peak}$ (mJy/beam)	$T_{\rm SB}$ (K)	*FWHP* (arcsec)	$\Theta_{\rm S}$ (arcsec)	S_ν (mJy)	rms (mJy/beam)
A	6	18:08:38.187	–19:51:49.52	16.4	2770	0.″85	0.″64	37	0.20
B1[a]	6	18:08:38.247	–19:51:50.22	6.7	1120	0.″55	–	11	″
B2[a]	6	18:08:38.222	–19:51:50.61	4.5	760	0.″55	–	4.5	″
A	3.6	18:08:38.186	–19:51:49.52	16.5	4050	0.″55	0.″48	62	0.059
B1	3.6	18:08:38.249	–19:51:50.23	11.1	2740	0.″31	0.″16	17	″
B2	3.6	18:08:38.222	–19:51:50.61	6.4	1570	0.″29	0.″12	7.8	″
D	3.6	18:08:38.274	–19:51:48.09	1.6	393	0.″29	0.″12	1.7	″
A	2	18:08:38.191	–19:51:49.44	52.0	990	0.″64	0.″35	75	0.74
B1	2	18:08:38.247	–19:51:50.13	30.2	580	0.″65	0.″37	42	″
B2	2	18:08:38.221	–19:51:50.55	18.0	340	–	–	18″	
A	1.3	18:08:38.186	–19:51:49.52	5.7	860	0.″67	0.″66	48	0.24
B1	1.3	18:08:38.243	–19:51:50.18	11.3	1720	0.″17	0.″12	28	″
B2	1.3	18:08:38.219	–19:51:50.59	9.6	1470	0.″14	0.″079	13	″

[a] All parameters obtained from 2D Gaussian fit, assuming two point-like sources.

Table 3. Observed parameters of the continuum sources in G31.41+0.31.

Source	λ (cm)	α(J2000)	δ(J2000)	$F_{\rm peak}$ (mJy/beam)	$T_{\rm SB}$ (K)	*FWHP* (arcsec)	$\Theta_{\rm S}$ (arcsec)	S_ν (mJy)	rms (mJy/beam)
A	3.6	18 47 34.305	–01 12 45.97	0.32	116	0.″22	–	0.32	0.033
B	3.6	–	–	<0.1	<36	–	–	0.11	″
A	1.3	18 47 34.306	–01 12 45.94	0.53	163	0.″108	0.″061	0.76	0.033
B	1.3	18 47 34.315	–01 12 45.81	0.35	106	0.″113	0.″069	0.46	″
A	0.7	18 47 34.305	–01 12 45.94	0.91	194	0.″071	0.″045	1.47	0.084
B	0.7	18 47 34.314	–01 12 45.80	0.70	150	0.″068	0.″039	0.88	″

one obtains a lower limit to the Lyman continuum luminosity $N_{\rm Ly} \simeq 5 \times 10^{45}$ s^{-1} and a spectral type B1 for the ionising star. This can also explain why G10 D is not detected at the other frequencies. If the free-free emission is optically thick below 3.6 cm and thin above it, the extrapolated fluxes at 6, 2, and 1.3 cm are 0.6, 1.6, and 1.5 mJy, respectively. Moreover, the source is slightly resolved by the 0.″11 beam at 1.3 cm, which decreases the peak flux to 1.3 mJy. All of these extrapolated values are below the 5σ upper limits of the corresponding images in Fig. 1, i.e., 1.1, 3.8, and 1.3 mJy/beam. We note also that the 1.3 cm images of Paper I and Paper II are not sensitive enough to detect a 1.5 mJy source.

In Paper II, no continuum emission had been detected towards the HMC in G31. The high sensitivity and resolution of our new images enable us to detect two compact sources in projection against the core. While for G10 it is possible to prove that A, B1, and B2 are embedded inside the HMC because of the NH_3 absorption observed towards them (see Paper II and Sect. 3.2), this is not feasible in the case of G31 because the two sources (denoted by A and B in Fig. 2) are insufficiently bright (see Table 3). Nonetheless, it is unlikely that the location of the two continuum sources close to the centre of the HMC is coincidental, so that in the following we assume that they are enshrouded by the dense, hot gas emitting the NH_3(4,4) line. Table 3 gives the main parameters of the two continuum sources. Since at 3.6 cm the resolution is insufficient to resolve the sources, at this wavelength the relevant parameters have been derived by fitting two 2D Gaussians. We note that each object appears to be barely resolved. Furthermore, as the G31.41+0.31 HMC is located within a region of extended continuum emission, the flux measurements (particularly at 3.6 cm) of the compact components carry large uncertainties. We postpone until Sect. 4.2.1 a discussion of the nature of G31 A and B.

3.2. Ammonia line

In Figs. 3 and 4, we compare the 1.3 cm continuum emission with that of the NH_3(4,4) transition, averaged under the main line and the satellites. There is little doubt that the HMCs are fully resolved and that compact continuum sources lie deeply embedded inside the cores, with the exception of G10 A, which is located close to the HMC surface. Despite the high angular resolution, only ~45% of the flux density measured in the main line with the D-array (see Paper I) is resolved by our A-array observations – consistent with the compactness of HMCs. We note that the main line flux is approximately the same in the D-, C-, and B-arrays (Papers I and II) and drops off only in the A-array. The flux in the satellite lines, however, changes very little between the B- and A-arrays. This is an indication that small dense condensations are embedded in a more extended, lower (column) density medium. This interpretation is supported by the clumpiness that can be seen in the ammonia maps in Figs. 5 and 6, and suggests that the gas is far from being smoothly distributed on scales as small as a few hundred AU.

Deep absorption towards the HC HII regions in G10 is observed. This had been already detected in Papers I and II, but our new data allow us to disentangle the absorption line arising from B1 from that arising from B2. We will make use of this fact in Sect. 4.1.2.

The top and middle panels of Fig. 5 show that deep absorption is detected towards the HC HII regions B1 and B2 in G10. The bottom panels display the ratio of the main line to satellite maps, which is close to unity, a proof that the NH_3 emission is very optically thick. As a consequence, the brightness temperature measured in the beam is an excellent approximation of the gas kinetic temperature (see also Sect. 4.1.2). We note how the main-line/satellite ratio is >1 towards B1 and B2,

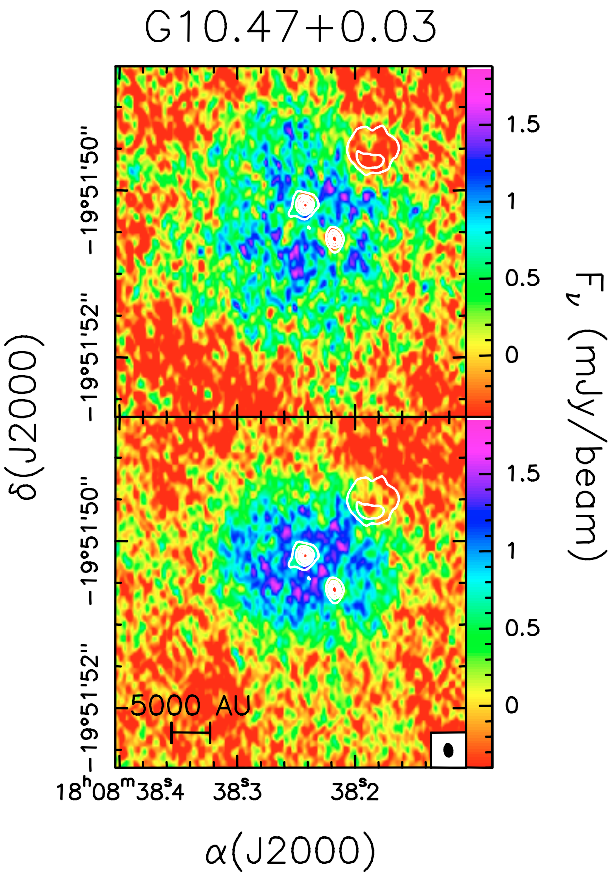

Fig. 3. *Top*: overlay of the 1.3 cm continuum map (contours, as in Fig. 1) on the image of the NH_3(4,4) emission averaged under the main line in G10. *Bottom*: same as above for the NH_3(4,4) emission averaged under the four satellites. Note that both colour scales have been clipped at −0.4 mJy/beam to enhance the contrast of the images. The ellipse at the bottom right denotes the synthesised beam of the ammonia maps.

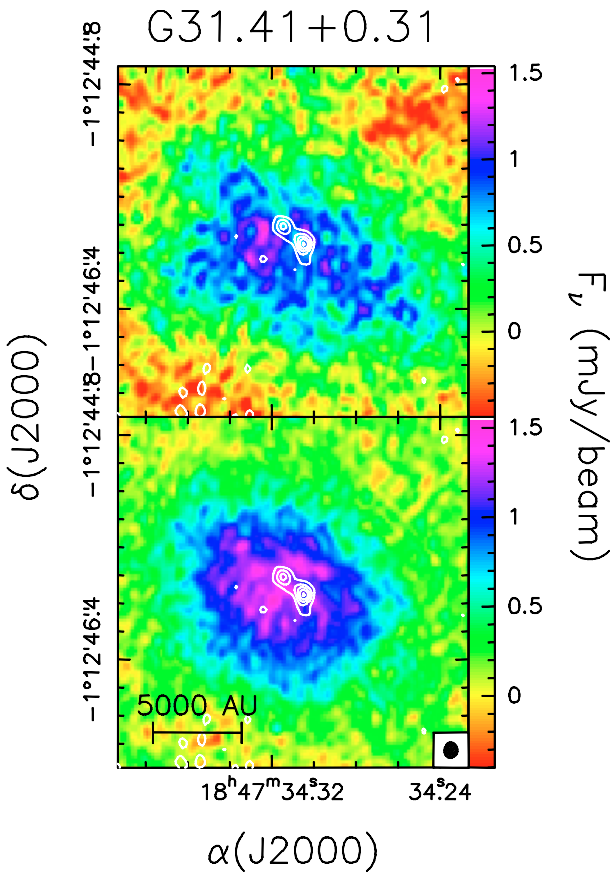

Fig. 4. *Top*: overlay of the 1.3 cm continuum map (contours, as in Fig. 2) in the image of the NH_3(4,4) emission averaged over the main line in G31. *Bottom*: same as above for the NH_3(4,4) emission averaged under the four satellites. The ellipse at the *bottom right* denotes the synthesised beam of the ammonia maps.

suggesting that the ammonia absorption is significantly more optically thin than the emission. In G31, the main line/satellite ratio is <1 over most of the HMC. This cannot happen if the core is homogeneous and isothermal therefore we conclude that the gas temperature must increase outside-in, as found by Beltrán et al. (2005). In this case, the main line emission, being more optically thick than the satellites, arises from layers closer to the surface – and hence colder – than the layers from which the satellite photons are emitted. This explains why the main line is fainter than the satellites. The existence of a temperature gradient will be directly established in Sect. 4.2.2.

Finally, we note that the shape of the main-line emitting cores is different in G10 and G31, the former being approximately circular and the latter elongated in the NE–SW direction. These different structures could be related to the different velocity fields in the two cores, as discussed in Sects. 4.1.2 and 4.2.2.

4. Discussion

We derive the relevant physical parameters of the continuum sources and HMCs and analyse our findings separately for each object.

4.1. G10.47+0.03

4.1.1. Nature of the continuum sources

Our previous derivation of the parameters of the HII regions and ionising stars in G10 (Papers I and II) assumed that we were dealing with classical Strömgren spheres, of low optical depth at the observing wavelength of 1.3 cm. Our knowledge of the continuum spectrum (especially for B1 and B2) was hindered by the limited angular resolution attained by previous images at other frequencies. Now, our new data at 3.6 cm and those retrieved from the VLA archive make it possible to establish the spectral energy distribution (SED) of all three HII regions and thus attempt a more sophisticated derivation of the physical parameters. We point out that the 1.3 cm flux used in the SED is not the one measured with the A-array, but that obtained from our previous B-array data, whose (u, v) sampling is more similar to those of the maps at longer wavelengths. The SEDs of A, B1, and B2 are shown in Fig. 7, where we also plot the corresponding best fits obtained with a spherically symmetric HII region with electron density $n_e \propto R^p$, where R is the distance from the star. This is basically the model outlined by Keto (2002) that depends on the HII region angular size, the index p, and the Lyman continuum luminosity, N_{Ly}, of the ionising star. We note that the assumed uncertainty of 15% in the flux density is to be taken as a lower limit, given the unknown amount of flux resolved in our interferometric observations.

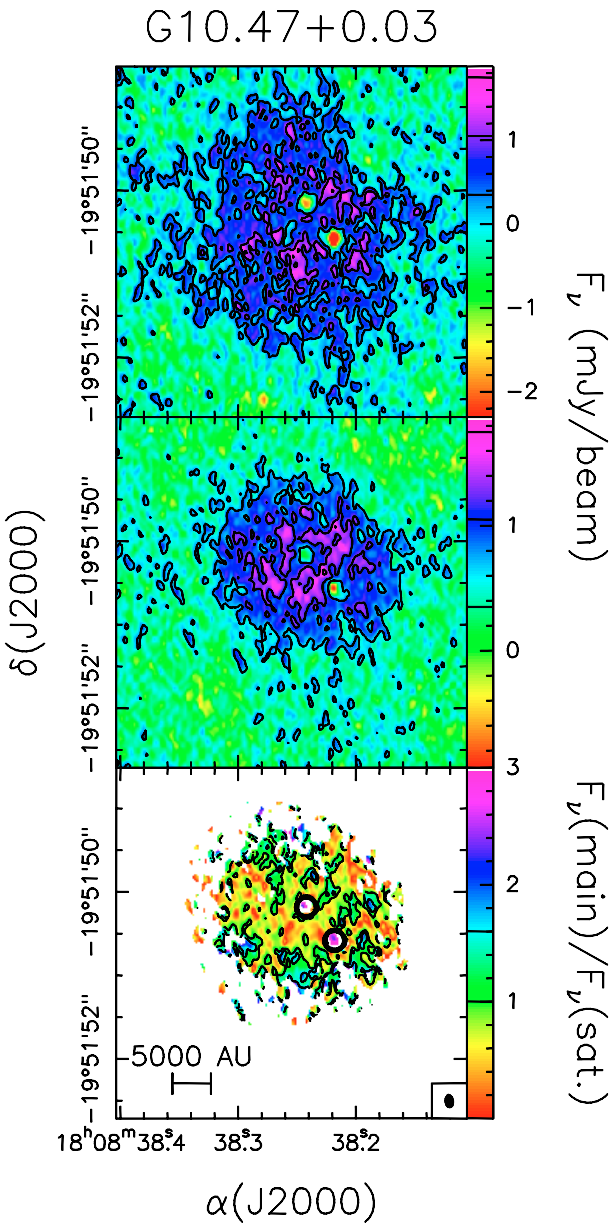

Fig. 5. *Top*: map of the NH_3(4,4) emission averaged under the main line in G10. *Middle*: map of the NH_3(4,4) emission averaged under the four satellites. *Bottom*: map of the ratio between the main line and satellite maps. A ratio <37 implies that the main line is optically thick, <1.6 that also the satellite emission is thick. Note that the maximum ratio is 5.8, but the colour scale has been clipped at 3 to enhance the contrast of the image. The two circles mark the positions of the HC HII regions B1 and B2. The values of the contours are marked in the colour-scale wedges to the right of each panel. The ellipse at the *bottom right* denotes the synthesised beam of the ammonia maps.

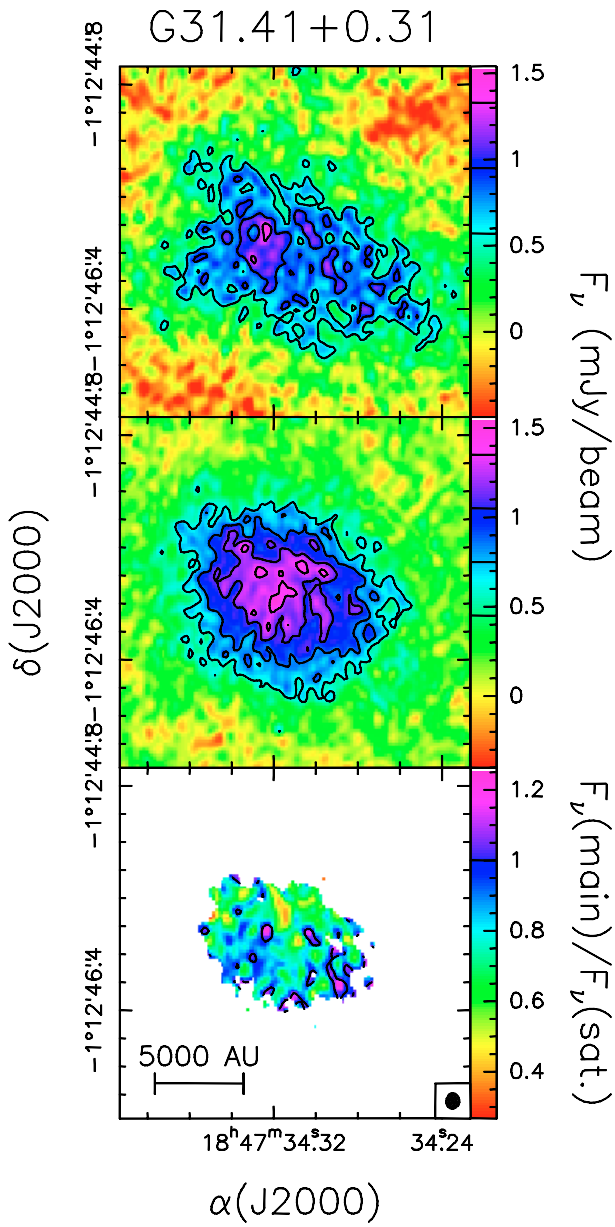

Fig. 6. *Top*: map of the NH_3(4,4) emission averaged under the main line in G31. *Middle*: map of the NH_3(4,4) emission averaged under the four satellites. *Bottom*: map of the ratio between the main line and satellite maps. A ratio <37 implies that the main line is optically thick, <1.6 that also the satellite emission is thick. The values of the contours are marked in the colour-scale wedges to the right of each panel. The ellipse at the *bottom right* denotes the synthesised beam of the ammonia maps.

The best fits shown in Fig. 7 were obtained by varying the three input parameters over a grid and taking those for which the minimum value of the quantity $\sum_i[\mathrm{Log}(S_{\nu_i}^{\mathrm{model}}) - \mathrm{Log}(S_{\nu_i}^{\mathrm{data}})]^2$ was attained. Only for G10 A have we assumed $p = 0$ a priori, since the UC HII region is clearly resolved and the brightness distribution is definitely not centrally peaked, as expected for a power-law density distribution. For B1 and B2, p was varied in the range $-1.5 \leq p \leq 0$, because for steeper density gradients, ionisation equilibrium is impossible (see Franco et al. 1990). The best-fit model parameters are given in Table 4, in addition to the spectral type of the corresponding zero-age main-sequence (ZAMS) star, obtained from N_{Ly} using Table 2 of Panagia (1973)[2]

It is interesting to compare our results with those given in Tables 3 and 4 of Paper II. First, we note that the angular diameter, Θ_{S}, obtained from our best fit is very similar to the diameter computed from the D+C+B combined maps of Paper II. This consistency provides support for our model. Another interesting result is that, even accounting for the different distance

[2] We prefer to use Panagia's estimates rather than more recent ones for the sake of consistency with Paper II. Note that the variation in the estimated spectral type would not be significant: e.g., using the results of Martins et al. (2002) would affect only the spectral type of G10 B2, which would change from O7.5 to O8.

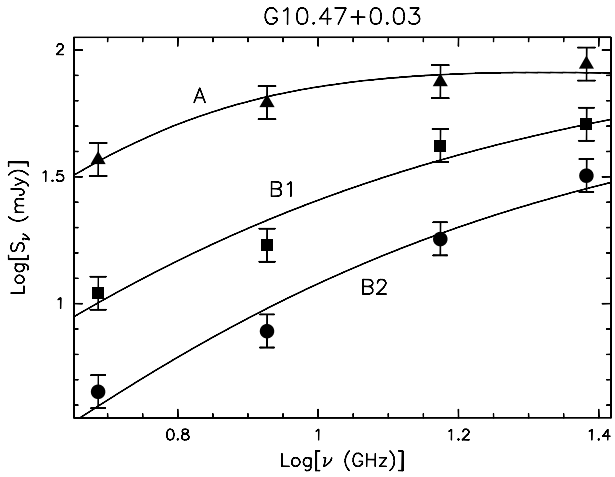

Fig. 7. Spectral energy distributions of the continuum sources detected in the G10 HMC. Note that the 1.3 cm flux is not the one given in Table 2 (where most of the emission is resolved out) but that obtained from our old B-array data. The errorbars allow for 15% calibration uncertainty. The curves represent the best fit to the data using a model of an HII region with a density gradient (see text).

Table 4. Parameters of the HII regions and corresponding ionising stars in G10.47+0.03. A distance of 10.8 kpc is adopted.

Name	Θ_S (arcsec)	p	N_{Ly} (s^{-1})	Spec.type
A	0.56	0^a	10^{48}	O9
B1	0.30	−1.5	5×10^{48}	O7
B2	0.18	−1.5	3×10^{48}	O7.5

[a] Assumed a priori (see text).

assumed here (10.8 kpc instead of 5.8 kpc), our spectral type estimates for B1 and B2 are earlier than those in Paper II, while that of A is only marginally later. This suggests that the embedded OB stellar population might be significantly more massive than expected assuming a constant density distribution for HC HII regions. Although difficult to quantify, this finding could have consequences for the mass function of young massive stars, provided their formation proceeds by means of accretion as depicted by Keto (2002, 2003). In his model, high-mass stars undergo Bondi-Hoyle accretion from the parental core *through* the HII region and the density gradient inside the so-called gravitational radius, R_G, is very close to the free-fall profile $n_e \propto R^{-1.5}$. With this in mind, that the SEDs of B1 and B2 appear to be more accurately reproduced by the density power law $n_e \propto R^{-1.5}$ lends support to Keto's model and indirectly indicates that also the surrounding molecular gas (i.e., the HMC) in G10 could be infalling. On the other hand, this power-law density profile is not to be taken as iron-clad evidence of infall. One cannot exclude the possibility that the observed density profile is determined by expansion of the HII region, since slopes as steep as −2 are known to be typical of ionised expanding shells (see e.g., Panagia & Felli 1975).

Assuming that the infall interpretation is correct, one may wonder whether the two HC HII regions gravitationally trapped by the infalling envelope. If this is the case, their radii should be less than the corresponding gravitational radii. The latter can be estimated using the expression $R_G = GM_\star/c_{II}^2$ (see e.g., Keto & Wood 2006), where G is the gravitational constant, $M_\star$ the mass of the star, and $c_{II} \simeq 13$km s^{-1} the isothermal sound speed in the ionised gas. For both B1 and B2, $R_G \simeq 0''.02$ is much smaller than the radii estimated by us. This suggests that, albeit still very compact, all HII regions in G10 are already in their expansion phase.

4.1.2. Structure of the HMC

In Papers I and II, we derived the global properties (e.g., mass, mean density) of the HMC in G10 and attempted to estimate the dependence of the temperature and velocity on the core radius. Here we take advantage of an increase by a factor 4 in angular resolution to improve on our previous analysis.

Given the approximate circular symmetry of the core, the best way to study the variation in the gas parameters with radius is to calculate the azimuthal average (in circular annuli) of the NH_3(4,4) line emission, using B1 as the centre. In Fig. 8, we show the position-velocity plot along the core radius, obtained in this way. Two considerations are in order. The first is that the main-line intensity is comparable to that of the satellites at almost all radii, which proves that the NH_3(4,4) line is optically thick all over the core. The second is that, apart from the blue-shifted absorption towards the centre (i.e., towards B1), the only other peculiarity in Fig. 8 is that the main line peaks at ~73 km s^{-1} for radii <0.″8 and close to the systemic velocity (~67 km s^{-1}) beyond that. That the line emission is skewed towards the red at an offset of 0.″5 from B1 is explained by the presence of blue-shifted absorption against B2, which is located at that distance from B1. We note that this effect is not evident in the satellites, which are less affected by absorption, and their peak velocity is basically the same at all radii.

In the following, we discuss all of these issues.

Velocity field: because the *HPBW* is similar in size to the HC HII regions, the absorption features are not contaminated by the nearby emission, which affected the absorption spectra in Paper II. We can thus obtain "pure" absorption spectra towards B1 and B2, and even more so towards A. These are shown in Fig. 9, overlayed on the fits obtained by taking into account the hyperfine structure of the ammonia inversion transition (see e.g., Paper I). Also shown, for the sake of comparison, is the mean line profile (in emission) over the entire core.

One sees that, while the velocity in A is basically the same as the systemic velocity obtained from emission lines (e.g., CH_3CN; see Olmi et al. 1996a, 1996b, Beltrán et al. 2005), in B1 and B2 the absorption is clearly blue-shifted. Since A is located very close to the HMC border along a line-of-sight tangent to the core itself, it is unsurprising that the absorbing gas has little or no velocity shift and a low column density, which is consistent with the non-detection of the satellites and the weakness of the main line.

In contrast, the strong, blue-shifted features in B1 and B2 indicate that the gas is *expanding*. In Sect. 4.1.1, we found that the density gradient inside the two HC HII regions indirectly suggests that the surrounding envelope could still be *infalling* towards the stars. How can one reconcile these two findings? We propose that the expanding gas is associated with two well-collimated molecular outflows that pierce the (infalling) HMC and are directed approximately along the line of sight.

In this scenario, one expects the column density to be greater in the infalling gas, representing the bulk of the HMC, than in the expanding outflow lobes, because infall compresses the gas whereas expansion disperses it. This is indeed consistent with the lower optical depth of the absorption lines, as indicated by the lower satellite/main line ratio observed towards B1 and B2

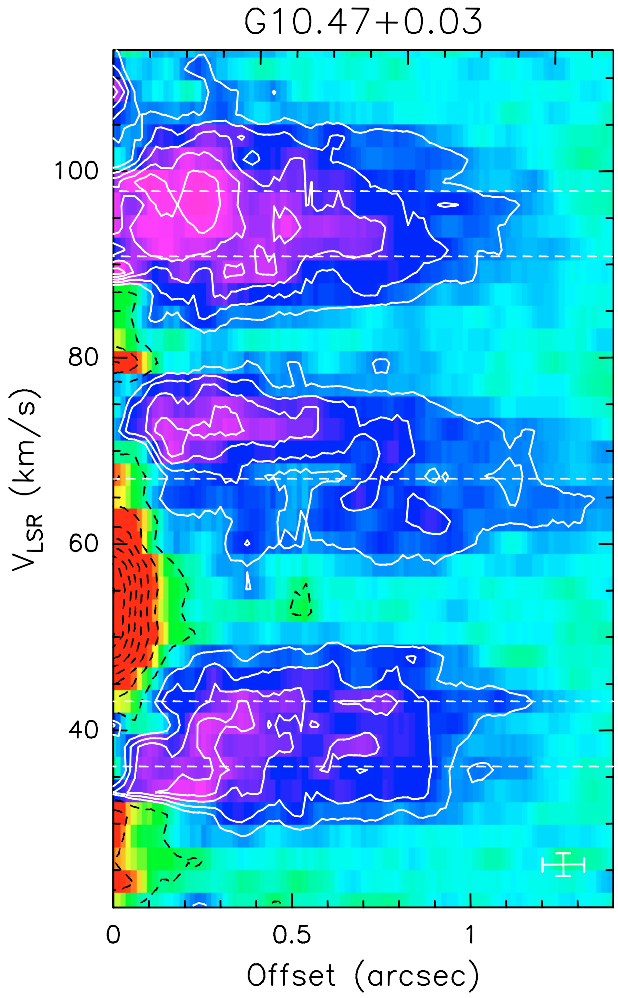

Fig. 8. Plot of the NH_3(4,4) line intensity as a function of LSR velocity and distance from the centre of the HMC in G10, assumed to coincide with the HC HII region B1. Contour levels range from −10.9 to −0.4 in steps of 1.5 mJy/beam and from 0.4 to 1.6 in steps of 0.3 mJy/beam. The dashed horizontal lines mark the positions of the main line and strongest satellites. The cross at the *bottom right* indicates the angular and spectral resolutions.

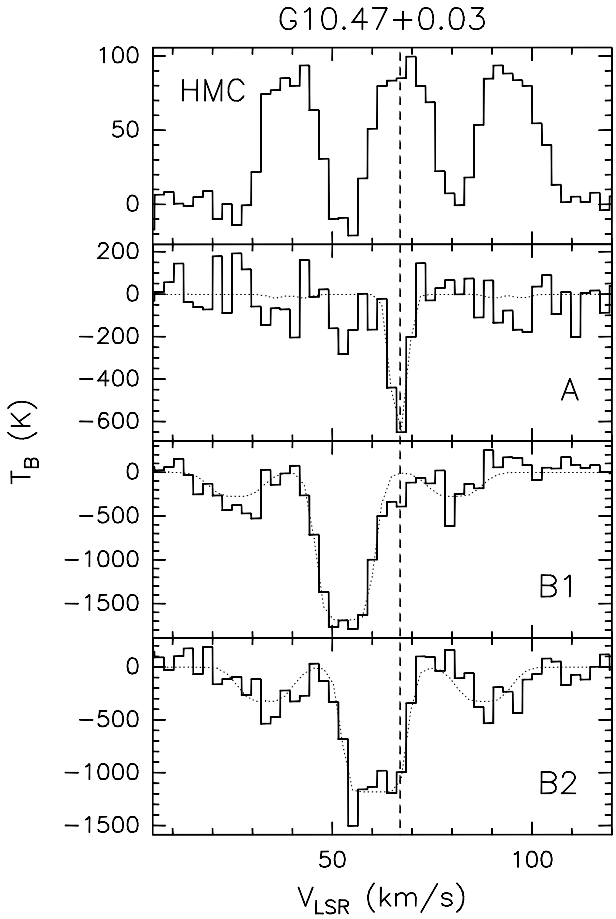

Fig. 9. Spectra of the NH_3(4,4) line towards G10.47+0.03. From *top to bottom*: mean (source averaged) spectrum over the HMC; beam-averaged spectra towards the absorption peaks of HII regions A, B1, and B2. The dotted profiles are the best fit obtained by taking into account the hyperfine structure. The dashed vertical line indicates the systemic velocity of the core.

with respect to that seen in the mean emission spectrum (see Fig. 9).

From the ratio of the intensity of the main-line to that of the satellites, one can obtain the optical depth of the NH_3(4,4) line and then estimate the total ammonia column density for a given kinetic temperature, assuming the gas to be in local thermodynamic equilibrium (see e.g., Ungerechts et al. 1986). Using this well established technique, from the fit to the absorption lines (similar to those in Fig. 9) we derive an ammonia column density of $N_{NH_3} \simeq 7 \times 10^{17}$ and 10^{18} cm^{-2} for B1 and B2, respectively. The corresponding H_2 column density, is obtained dividing N_{NH_3} by the ammonia abundance relative to H_2, X_{NH_3}, which is very uncertain. The value quoted e.g., by Van Dishoek et al. (1993) for the Orion hot core is 10^{-7}, much less than that obtained in Paper I for G10, 10^{-5}. However, the latter value refers to the HMC, whereas ammonia is expected to be much less abundant in the outflow component. Here we assume that $X_{NH_3} = 10^{-6}$ and caution that there is a large uncertainty. In our calculation, we also adopt a kinetic temperature of 100 K, as suggested by the peak T_B of the mean NH_3(4,4) spectrum (see top panel of Fig. 9). Assuming that the velocity of the expanding gas, V_{out}, is equal to the difference between the velocity of the absorption feature and the systemic velocity (~13.7 km s^{-1}), one can estimate the dynamical timescale of the outflow to be $t_{out} = R_{NH_3}/V_{out} \simeq 5{\times}10^3$ yr, where $R_{NH_3} \simeq 0.07$ pc is the radius of the HMC. The outflow mass loss rate is then obtained from the expression

$$\dot{M}_{out} = 2 \times \frac{\pi}{4}(\Theta_S\, d)^2 \frac{N_{NH_3}}{X_{NH_3}} \frac{m_{H_2}}{t_{out}}, \quad (1)$$

where d is the distance, m_{H_2} the mass of the H_2 molecule, Θ_S is given in Table 2, and the factor 2 accounts for us being able to see only one of the two outflow lobes in absorption. The total mass-loss rate from B1 and B2 is ~2.5×10^{-4} $M_\odot$ yr^{-1}, while the momentum rate is $\dot{M}_{out}\, V_{out} \simeq 3 \times 10^{-3}$ $M_\odot$ km s^{-1} yr^{-1}. The latter compares well to the momentum rate obtained for the large-scale outflow imaged towards G10 with the 30-m Pico Veleta telescope in the ^{13}CO line (López-Sepulcre et al. 2009). We note that our estimates are likely to be lower limits, because we have assumed that only the gas seen in absorption belongs to the outflow.

Based on the previous considerations, we conclude that both infall and expansion could coexist in G10 HMC, the former involving most of the core gas, the latter being confined to narrow bipolar outflows from B1 and B2.

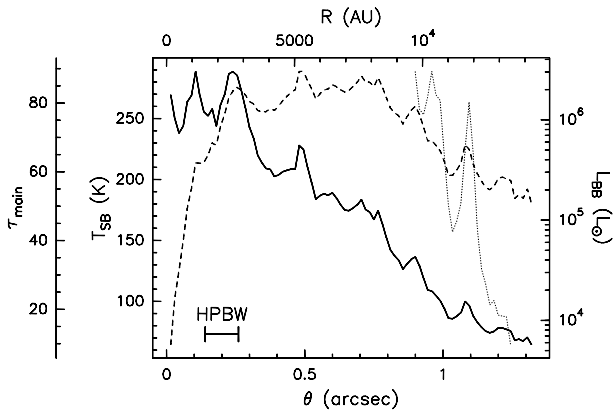

Fig. 10. The solid curve is a plot of the NH_3(4,4) line synthesised beam brightness temperature as a function of core radius in G10; the error in this curve equals the 1σ rms noise in Fig. 8, namely 16 K. The dashed curve is the luminosity of a spherical black body with radius R and temperature $T_{SB}(R)$. The dotted curve represents the optical depth of the main line; this could be calculated only at sufficiently large radii, where the satellite to main line ratio is significantly <1. The angular resolution is indicated by the bar at *the bottom left*.

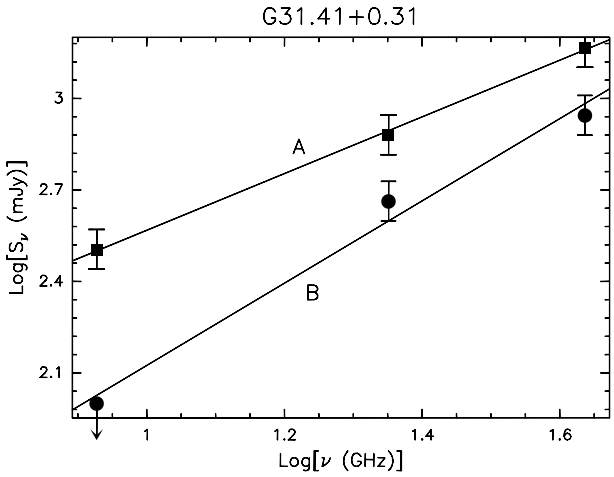

Fig. 11. Spectral energy distributions of the continuum sources detected in the G31 HMC. The errorbars represent a 15% calibration uncertainty. The straight lines are least square fits to the data of the type $S_\nu \propto \nu^\alpha$, where $\alpha = 0.9$ and 1.3 for A and B, respectively.

Temperature and luminosity: using Fig. 8, one can obtain the temperature profile inside the HMC by plotting the maximum T_{SB} measured across the line profile (including the satellites) as a function of distance from the HMC centre (solid line in Fig 10). This method is justified by, as already noted, the ratio of main line and satellites indicating that the NH_3(4,4) line is optically thick all over the core. This is shown in Fig. 10 where the dotted curve represents the main-line optical depth. Clearly, the opacity of the main line is $\tau_{main} \gg 1$ at all radii. As already discussed in Papers I and II, at the high densities typical of HMCs the ammonia inversion transitions are thermalised. Local thermodynamic equilibrium conditions and high optical depths imply that the peak brightness temperature can be used as an excellent approximation to the kinetic temperature of the gas.

Clearly, the temperature increases outside-in. This increase appears to be inconsistent with the high optical depth of the NH_3(4,4) line: if the core is optically thick, only the surface should be visible and the observed T_{SB} should be more or less the same at all radii. The reason why we observe a temperature variation is probably because of clumpiness and large velocity gradients in the gas, which allow us to glimpse beneath the HMC surface. However, this effect is diminished to some extent at the highest column densities, which explains why T_{SB} tends to flatten at small radii. This flattening is also caused by beam dilution and to some emission being "eaten" by the absorption towards B1.

With this in mind, we may consider the T_{SB} profile in Fig. 10 as a lower limit to the effective kinetic temperature inside the HMC. As shown in Paper II, we now calculate the luminosity of the HMC and compare this with other estimates. We use the approximation of a spherical black body, whose luminosity equals $L_{BB} = 4\pi R^2 \sigma T^4$. As we have seen, T_{SB} is a reasonable approximation for T. The problem is to establish which radius can be used as the "photosphere" of the black body. As noted in Paper I, this depends on the dust opacity in the mid-IR, where the bulk of the black-body luminosity is emitted (the SED of a ~100 K black body peaks at 30 μm). Since a priori this radius is unknown, we calculate L_{BB} at all radii at which T_{SB} has been measured (dashed line in Fig. 10). To constrain the value of R, we use the lower and upper limits to the luminosity of G10 given, respectively, by the sum of the luminosities of the embedded stars (of spectral types O7 and O7.5, corresponding to $\sim 2 \times 10^5\ L_\odot$) and the luminosity of the associated IRAS point source ($7\times10^5\ L_\odot$). The corresponding range spanned by R is 0.″9–1.3″.

We conclude that the luminosity of the HMC is very likely to be a few times $10^5\ L_\odot$ corresponding to an effective radius of 0.05–0.07 pc.

4.2. G31.41+0.31

4.2.1. Nature of the continuum sources

We now investigate the nature of the previously undetected continuum sources A and B in the G31 HMC. Figure 11 shows their spectra, which one can attempt to fit with the model already used in Sect. 4.1.1. However, unlike the case of G10, the angular diameters obtained from the fit to the SEDs are ≥0.″5, an order of magnitude larger than those measured in the continuum map (≲0.″07; see Table 3). This strongly suggests that the hypothesis that A and B are HII regions is wrong and we decided not to use this model fit. An alternative possibility is that the observed emission originates in thermal jets. It is well known that such jets have SEDs resembling power laws with slopes up to 1.5 (see e.g. Anglada 1996), i.e., similar to those in Fig. 11. Moreover, jet models predict that the angular size should decrease with increasing frequency as a power law with an index that is found to vary with the jet opening angle. Anglada's values range from −1.9 to −0.3. Using the 1.3 cm and 7 mm data in Table 3 (the resolution at 3.6 cm is insufficient to estimate the source size), we obtain indices of −0.46 and −0.87, respectively, for A and B, which further support the jet model.

If the jet interpretation is correct, what are the masses of the powering stars? To answer this question one can use the parameter $S_\nu d^2$, which is an estimate of the emission strength of the jet used to relate the observed jet properties to the relevant physical parameters of the powering source. For G31 A and B, we have $S_\nu d^2 \gtrsim 7$ mJy kpc^2, which is much higher than the values found by Anglada (1996) in their sources, namely $S_\nu d^2 < 1$ mJy kpc^2. Since the latter sample comprises mostly low- and intermediate-mass YSOs, we conclude that our objects are high-mass YSOs.

Extrapolating the trend in Fig. 4 of Anglada (1996), we can derive a rough estimate of the momentum rate of the jets: this

is ∼0.03−0.06 $M_\odot$ km s^{-1} yr^{-1}, typical of high-mass YSOs (see Wu et al. 2004 and López-Sepulcre et al. 2009). Values that high are consistent with the HMC luminosity obtained in Sect. 4.2.2 ($\lesssim 10^5$ $L_\odot$).

4.2.2. Structure of the HMC

Velocity field: as already noted in Sect. 3.2, the shape of the ammonia core in Fig. 6 is significantly elongated in the NE–SW direction. The existence of a velocity gradient in this direction was established by several authors (Cesaroni et al. 1994b; Paper II; Maxia et al. 2001; Beltrán et al. 2004, 2005; Gibb et al. 2004; Araya et al. 2008), who observed the G31 HMC at lower angular resolution than ourselves. To verify their results, in Fig. 12 we show a map of the first moment of the NH_3(4,4) main line. Clearly, the velocity is increasing from NE to SW, approximately from 92 to 102 km s^{-1} over 1.″6, corresponding to a velocity gradient of ∼160 km s^{-1} pc^{-1}. For comparison, in Paper II we found a value ∼2 times smaller over a region ∼2 times larger, while velocity gradients of 26 km s^{-1} pc^{-1} (over 3.″4) and 31 km s^{-1} pc^{-1} (over 5″) were measured, respectively, from the CH_3CN(12–11) (Beltrán et al. 2005) and H_2S (2_{20}−2_{11}) (Gibb et al. 2004) lines.

Comparing results obtained for different tracers and with different angular and spectral resolutions may lead to erroneous conclusions, and indeed the spread among the previous estimates is quite large. However, one should note that the velocity gradient obtained from our A-array measurements is by far the largest: this suggests that additional improvement in angular resolution might detect an even greater velocity spread over a smaller region. A velocity increasing with decreasing radius is indicative of conservation of angular momentum (or centrifugal equilibrium) in a rotating core. This interpretation was proposed by Beltrán et al. (2004, 2005), who modeled the CH_3CN(12−11) line emission with a rotating, infalling toroid. An alternative scenario was presented by Araya et al. (2008), who interpreted their CH_3OH observations as a bipolar outflow powered by a source lying between G31 A and B. We note that the argument of velocity increasing with decreasing radius is insufficient to discard the outflow interpretation, as the highest expansion speed is likely to occur close to the powering source.

Is it possible to discriminate between these two hypotheses (rotation versus expansion) on the basis of our new ammonia data?

To provide a more quantitative description of the velocity field in the G31 HMC, in Fig. 13 we show the position-velocity plot of the NH_3(4,4) line emission along a direction with PA = 45°. To increase the signal-to-noise ratio, we averaged the emission of the HMC along the perpendicular direction, i.e., along PA = −45°. The velocity change with offset is also seen in this plot, most clearly in the main line emission, because the satellite emission is affected by blending between the two strongest hyperfine components inside each pair of satellites. Focusing our attention on the main line, the shape of the plot is clearly asymmetric along the velocity axis, with the blue-shifted emission being more prominent than the red-shifted one.

This is also consistent with the blue-shifted velocities observed towards the centre of Fig. 12, because the first moment of the line is affected by the lack of red-shifted emission. This can be understood by looking at the NH_3(4,4) spectrum obtained by averaging the emission over the HMC (Fig. 14). Here the main line peak is skewed to the blue side, as expected in collapsing optically thick envelopes. Red-shifted self-absorption can explain this asymmetry (see e.g., Myers et al. 1996 and references

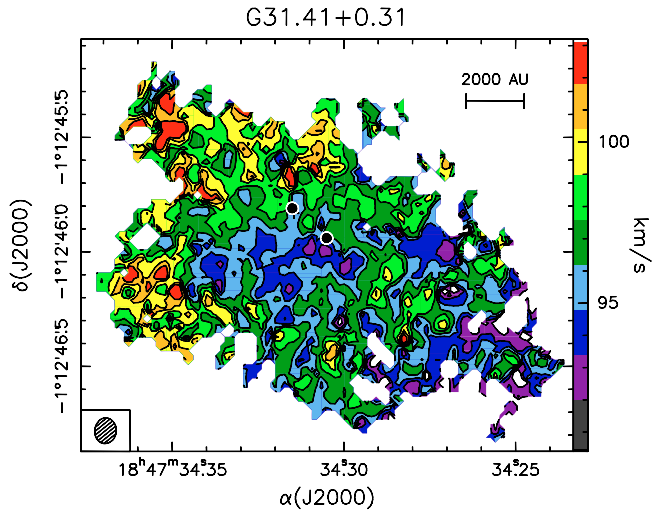

Fig. 12. Map of the first moment of the NH_3(4,4) main line in G31. The contour levels range from 92 (blue) to 101.8 (red) in steps of 1.4 km s^{-1}. The two black dots mark the positions of the continuum sources A and B. The ellipse at the bottom left denotes the synthesised *HPBW*.

therein) thus suggesting that the HMC is undergoing infall (and rotation), as hypothesised by Beltrán et al. (2005).

This effect is most evident when studying the shapes of NH_3(4,4) spectra across the core. To enhance self-absorption to the detriment of the NE–SW velocity gradient, we computed mean spectra at radius multiples of 0.″1 by averaging the emission over circular annuli centered on the position of B1. These are shown in Fig. 15. One can see that towards the HMC centre the ammonia main line becomes heavily self-absorbed, becoming even weaker than the (optically thinner) satellites. Moving outward, the main line to satellite ratio increases, and the red-shifted self absorption in the main line disappears.

As demonstrated in the Appendix, a ring of molecular gas undergoing infall and rotation is described by the expression

$$V_{\rm LSR} = V_{\rm sys} + V_{\rm rot}\frac{x}{R} \pm V_{\rm inf}\sqrt{1-\left(\frac{x}{R}\right)^2}, \qquad (2)$$

where $V_{\rm sys}$ is the systemic velocity (97 km s^{-1}), $V_{\rm rot}$ the rotation velocity, $V_{\rm inf}$ the infall velocity, x the offset as measured in Fig. 13, and R the ring radius. In a position-velocity plot, this equation describes an ellipse, as shown in Fig. 13. This ellipse was obtained for rotation and infall velocities both equal to 4 km s^{-1}, a radius of 0.″8 (or 0.03 pc), a systemic velocity of 97 km s^{-1}, and an infall/rotation centre coincident with the continuum source G31 A. As already pointed out, the weaker emission on the red-shifted side of the ellipse can be explained by self-absorption.

One can estimate the mass infall rate using the mean density estimate from Paper I ($n_{\rm H_2} \simeq 8.6\times10^6$ cm^{-3}) and the values of the infall velocity and corresponding radius obtained from the fit to the position–velocity plot. We have $\dot{M} = 4\pi R^2 m_{\rm H_2} n_{\rm H_2} V_{\rm inf} \simeq$ 0.019 $M_\odot$ yr^{-1}. This value lies in the range 3×10^{-3}–3×10^{-2} $M_\odot$ yr^{-1} derived by Girart et al. (2009) from the inverse P-Cygni profile of the $C^{34}S$(7–6) line, but is an order of magnitude greater than the value of 3×10^{-3} $M_\odot$ yr^{-1} obtained by Osorio et al. (2009). The latter is likely to be more reliable, as it was obtained by a model fitting to the NH_3(4,4) line profiles and the SED of the G31 region, whereas in our calculation of $\dot{M}$ we used only approximate values of the radius and density at which the infall velocity is measured. In any case, we note that

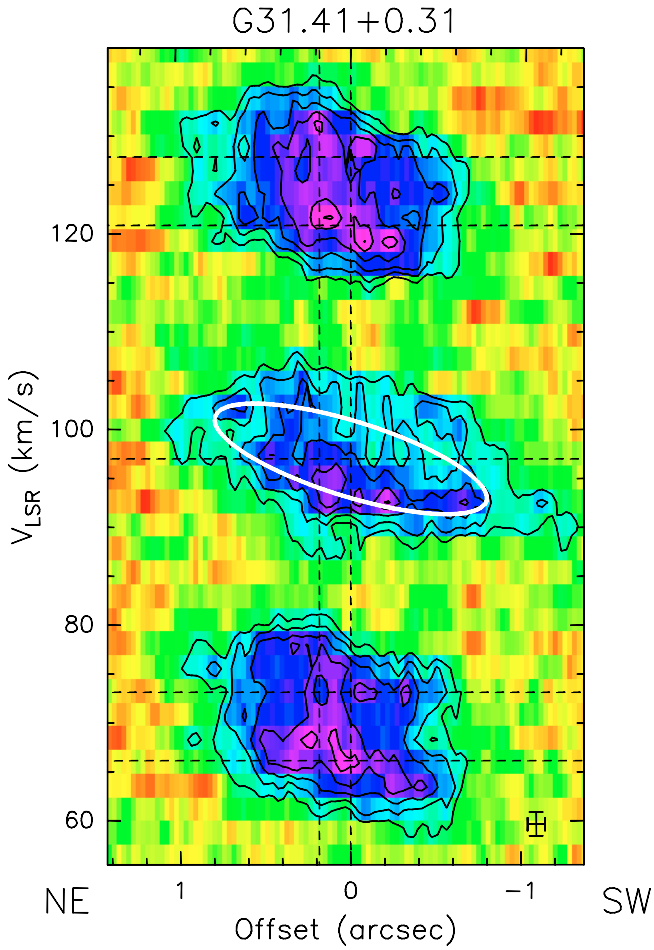

Fig. 13. Plot of the NH_3(4,4) line intensity as a function of LSR velocity and distance measured along the direction with PA = +45°. Zero offset corresponds to the position of the continuum source A. The emission has been averaged along the perpendicular direction (i.e., PA = −45°). Contour levels range from 0.4 to 1.4 in steps of 0.2 mJy/beam. The white ellipse corresponds to the locus of emission expected for a rotating and infalling shell of gas (see text). The dashed horizontal lines mark the positions of the main line and strongest satellites, while the vertical ones indicate the position of the two continuum sources A and B. The cross at the bottom right indicates the angular and spectral resolutions.

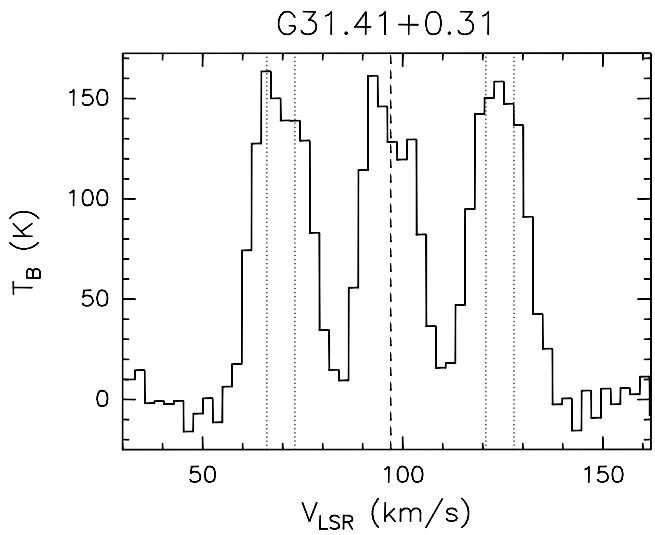

Fig. 14. Mean spectrum of the G31 HMC, obtained by averaging the NH_3(4,4) line emission inside the 3σ contour level of the main line map shown in the *top panel* of Fig. 6. The dashed line marks the systemic LSR velocity (i.e., the centre of the main line) and the dotted lines indicate the positions of the strongest satellites.

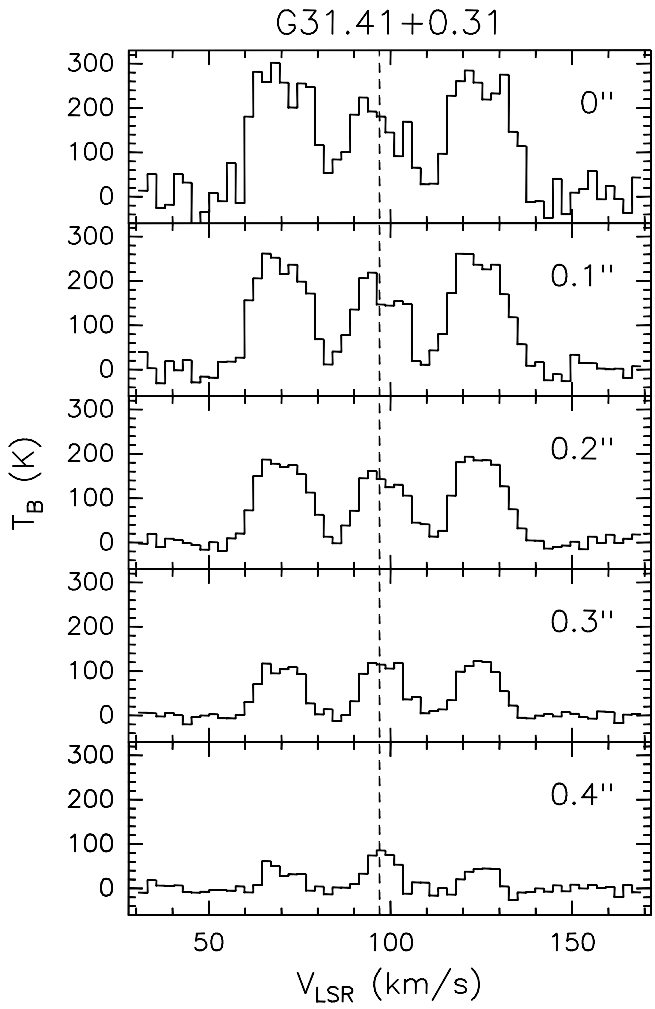

Fig. 15. Mean spectra of the NH_3(4,4) line in G31. Each spectrum refers to the angular distance from the core centre indicated in the *top right* of the corresponding panel. The dashed vertical line marks the systemic velocity. Note how the main line is heavily self-absorbed towards the HMC centre.

accretion rates $\lesssim 10^{-2}$ $M_\odot$ yr^{-1} are not unusual in high-mass star-forming regions (see e.g., Fontani et al. 2002; Zhang et al. 2005; Beltrán et al. 2006).

In this picture, part of the infalling material accretes onto the two continuum sources, A and B, which are aligned along the plane of rotation because they form a loose binary system formed at the centre of the HMC, rotating about the same axis as the core. This finding would be consistent with the prediction of Krumholz et al. (2009). According to their numerical simulations, high-mass stars form by means of disk accretion and fragmentation of the disk yields a massive stellar companion to the primary star.

Albeit appealing, this explanation cannot exclude the outflow hypothesis. Expansion does not exclude infall, if the outflowing NH_3 gas is ejected by a star that is at the same time accreting material from a compact NH_3 core. In this scenario, the self-absorbed NH_3 profile is caused by the infalling core, whereas the velocity gradient is caused by the expanding gas in the outflow. Other lines of evidence support the existence of an outflow in the region (see Araya et al. 2008 for a detailed

discussion), such as the similar velocity gradients being measured in the SiO(2–1) and HCO^+(1–0) lines (Maxia et al. 2001), which are well known jet/outflow tracers.

In this context, the two continuum sources A and B could be seen as the (unresolved) bow shocks at the two opposite ends of a thermal jet emanating from a star lying between them. The remarkable alignment between the A−B axis and the direction of the velocity gradient supports this hypothesis.

Assuming that we indeed observe a bipolar outflow lying close to the plane of the sky, it is possible to estimate the main outflow parameters from the gas mass associated with the NH_3 high-velocity emission, the separation between the blue- and red-shifted gas, and the corresponding velocities. As one can see in Fig. 14, only ~20% of the NH_3(4,4) emission is contained in the line wings. Assuming that the temperature of the gas traced by the NH_3(4,4) line is approximately the same at all velocities, this implies that only ~20% of the core mass is undergoing expansion. The most reliable HMC mass estimate is probably one obtained from the millimeter dust continuum (see Beltrán et al. 2004) i.e. ~490 $M_\odot$. From Fig. 13, one can estimate an outflow size and an expansion speed, respectively, of ~0.″8 (or 0.03 pc) and ~4 km s^{-1}, corresponding to a timescale of ~7300 yr. This is likely to be an upper limit because of the outflow inclination with respect to the line of sight. The mass and momentum rates are hence >1.3×10^{-2} $M_\odot$ yr^{-1} and >$5.4 \times 10^{-2} M_\odot$ km s^{-1} yr^{-1}. Albeit large, values such as these can be attained in the most luminous star-forming regions (see e.g., López-Sepulcre et al. 2009).

In conclusion, on the basis of our new data we cannot decide whether the velocity gradient observed in G31 is due to rotation or expansion, and the debate is bound to remain open until complementary information becomes available. The polarization study by Girart et al. (2009) indicates that the magnetic field lines describe a hour-glass-shaped structure aligned SE−NW, which is consistent with the rotating toroid interpretation. Future proper motion measurements of the maser spots associated with the HMC will help us to reconstruct the 3-D velocity field of the gas, thus helping to resolve this controversy.

Temperature and luminosity: we now proceed as for G10 to estimate the temperature profile and the luminosity of G31. Figure 16 shows the brightness temperature and the corresponding L_{BB} as a function of distance from the HMC centre, in an analogous way to Fig. 10. The difference with respect to G10 is that, due to the elongated morphology of the G31 core, we refrained from making an azimuthal average of the line emission and preferred to average it along the SE–NW direction, i.e., orthogonally to the major axis of the HMC. We then considered the maximum brightness temperature of each spectrum at different distances from G31 A. This is the solid curve in Fig. 16.

It is not worth repeating the considerations made in Sect. 4.1.2, which apply to G31 as well as to G10. Here, we note only that the temperature in the outer regions is similar for the two HMCs, but the increase towards the centre is apparently steeper in G31 than in G10, probably due to the lack of absorption in G31 against bright embedded continuum sources. The luminosity of the IRAS point source associated with G31 is 2.6×10^5 $L_\odot$, which also includes the O6 star ionising the UC HII to the NE of the HMC, namely 1.8×10^5 $L_\odot$ (see Table 5 and Fig. 3d of Paper II). Hence, the HMC luminosity must be $\lesssim 10^5$ $L_\odot$. This value is similar to the estimate obtained by Osorio et al. (2009) by model fitting the SED of the HMC and the NH_3(4,4) line profiles observed in Papers I and II. Using the same argument as for G10, we conclude that the radius of the photosphere emitting the bulk of the HMC luminosity is of order 1″ or 0.038 pc.

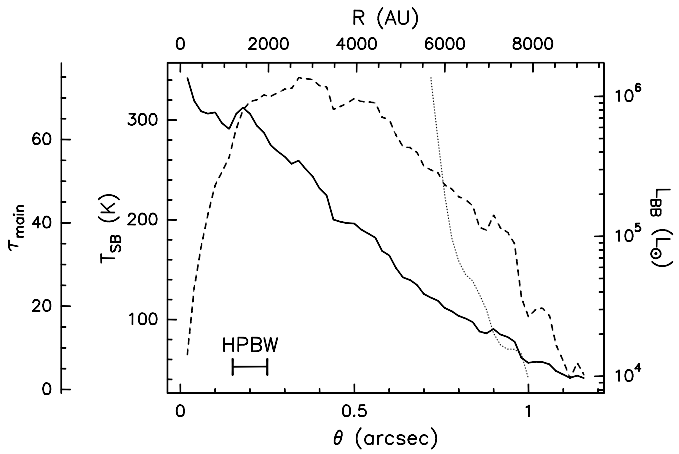

Fig. 16. Same as Fig. 10 for G31. The error in T_{SB} is 26 K, i.e., the 1σ rms in Fig. 13.

Table 5. Summary of the characteristics of the HMCs in G10.47+0.03 and G31.41+0.31. A "–" indicates that we do not have evidence in favour or against the corresponding issue.

HMC	HC HII	Ionised jet	Molecular outflow	Infall	Rotation
G10	Y	N	Y	Y	–
G31	N	Y	Y?	Y	Y?

5. Summary and conclusions

VLA A-array observations of the NH_3(4,4) line and continuum emission at various wavelengths have made it possible to shed light on the nature of the HMCs G10 and G31. Our main results are that G10 contains two deeply embedded HC HII regions (B1 and B2) associated with O9 ZAMS stars and an UC HII region (A) ionised by a B0 star located close to the HMC surface. Two weak continuum sources (A and B) have been detected inside the G31 HMC. The SEDs and the dependences of size on frequency are consistent with these sources being thermal radio jets powered by high-mass stars, rather than HII regions.

We obtain evidence of infall in both HMCs, but only in G10 do we detect expansion, possibly in two narrow bipolar outflows oriented along the line of sight. Nonetheless, we cannot exclude that the radio jets in G31 are associated with larger scale bipolar outflows, undetected in our ammonia observations.

The morphology and kinematics differ significantly from one HMC to the other. G10 appears to be spherical and to have no velocity gradient in the plane of the sky. In contrast, G31 is elongated NE–SW and the gas velocity increases systematically from SW to NE, while the NH_3(4,4) main line presents red-shifted self absorption. While two competing models have been proposed to interpret this feature (rotation versus outflow), we conclude that on the basis of our data neither hypothesis can be ruled out.

The temperature structure of the two cores indicates that the total luminosity of the embedded stars is of the order of 1×10^5–7×10^5 $L_\odot$, emitted mostly at a radius of 0.04–0.07 pc.

In Table 5, we summarize and compare the main properties of the two HMCs. Despite the similarities, one can see a few noticeable differences. Here, we attempt to elaborate a simple scenario accounting for them. In particular, one striking difference is that no detectable HII region is present in G31, although the luminosity (and the HMC mass; see Paper I) of the latter is only a few times less than that of the former. Why is this so? We can imagine two possible explanations:

(i) G10 is older than G31. In this case, the embedded early-type stars in the latter object are in a pre-HII region phase, which is why we detect only faint radio emission from them.
(ii) The most massive stars in G31 are less massive than those in G10. This may occur if, for purely statistical reasons, the initial mass function (IMF) in G31 is biased towards low stellar masses.

The latter scenario is unlikely. In Sect. 4.2.1, we have seen that the free-free emission from G31 A and B is much stronger than expected for a thermal jet from low- or intermediate-mass stars. This proves that, albeit not (yet) associated with HII regions, the stars in A and B are massive.

The former hypothesis, instead, is consistent with our findings. In particular, the lack of a HC HII region can be justified by the presence of accretion at a rate sufficiently high to trap the ionised gas (Keto 2002) or even inhibit its formation (Yorke 1985). We note that the rate of ~0.019 $M_\odot\,\mathrm{yr}^{-1}$ estimated in Sect. 4.2.2 is enough to quench an HII region around any early-type star, provided that the accretion has spherical symmetry.

If our interpretation is correct, one can speculate that G31 is in an earlier evolutionary phase than G10, when heavy accretion from a rotating/collapsing envelope onto a newly formed high-mass (proto)star is going on. At this stage, a thermal jet develops before the star is capable of ionising its molecular surroundings.

G10 could instead represent a later evolutionary phase, when the accreting material is partly diverted into a dense collimated jet digging its way through the parental core. Following Keto (2007), the presence of lower density channels and the increased stellar mass could allow the development of an untrapped HC HII region, which is bound to expand and eventually destroy the HMC.

Although highly speculative, the scenario depicted above is consistent with all of our findings. We believe that answering the questions concerning the nature and age of HMCs will not take too long. With the advent of ALMA, the number of observable tracers will increase enormously, as well as the angular and spectral resolution attainable. These dramatic improvements will provide us with suitable tools to solve the problem of high-mass star formation.

Acknowledgements. It is a pleasure to thank Maite Beltrán for critically reading the manuscript. P.H. acknowledges partial support from NSF grant AST-0908901.

Appendix A: Line-of-sight velocity of rotating ring

The purpose of this Appendix is to derive the expression of the velocity along the line of sight of a rotating and infalling ring seen edge-on. In Fig. A.1, a sketch of the ring of radius R and associated rotation ($V_{\rm rot}$) and infall ($V_{\rm inf}$) velocities is shown. The velocity measured by an observer located at $y = -\infty$ is the sum of the components along z of $V_{\rm rot}$ and $V_{\rm inf}$, plus the systemic velocity of the whole ring with respect to the local standard of rest ($V_{\rm sys}$):

$$V_{\rm LSR} = V_{\rm rot}\cos\phi - V_{\rm inf}\sin\phi + V_{\rm sys}. \quad (A.1)$$

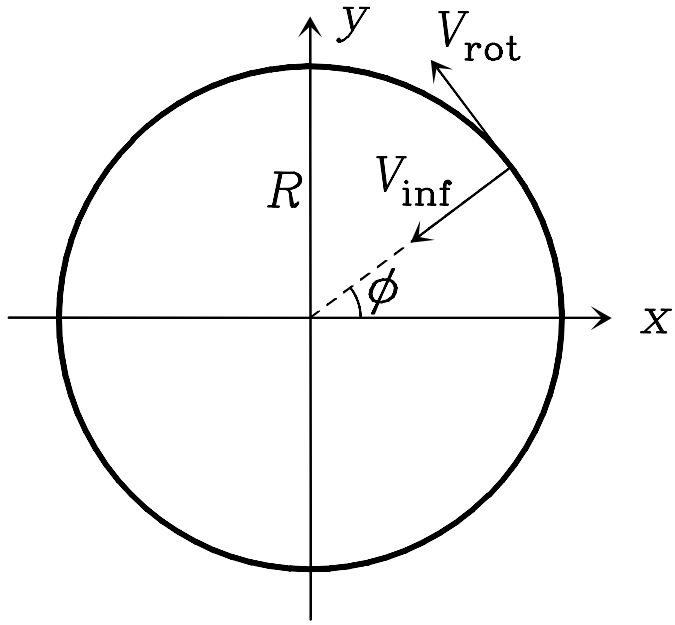

Fig. A.1. Sketch of a rotating and infalling ring of radius R seen edge on by an observer located at $y = -\infty$.

Using the expressions $\cos\phi = x/R$ and $\sin\phi = y/R = \pm\sqrt{R^2 - x^2}/R$, the previous equation becomes

$$V_{\rm LSR} = V_{\rm sys} + V_{\rm rot}\frac{x}{R} \pm V_{\rm inf}\sqrt{1 - \left(\frac{x}{R}\right)^2}. \quad (A.2)$$

References

Anglada, G. 1996, ASP Conf. Ser., 93, 3
Araya, E., Hofner, P., Kurtz, S., Olmi, L., & Linz, H. 2008, ApJ, 675, 420
Beltrán, M. T., Cesaroni, R., Neri, R., et al. 2004, ApJ, 601, L187
Beltrán, M. T., Cesaroni, R., Neri, R., et al. 2005, A&A, 435, 901
Beltrán, M. T., Cesaroni, R., Codella, C., et al. 2006, Nature, 443, 427
Beuther, H., Churchwell, E. B., McKee, C. F., & Tan, J. C. 2007, in Protostars and Planets V, ed. B. Reipurth, D. Jewitt, & K. Keil (Tucson: Univ. of Arizona Press), 165
Cesaroni, R. 2005, in Massive Star Birth: a Crossroads of Astrophysics, ed. R. Cesaroni, M. Felli, E. Churchwell, & M. Walmsley (Cambridge University Press), IAU Symp., 227, 59
Cesaroni, R., Churchwell, E., Hofner, P., Walmsley, C. M., & Kurtz, S. 1994a, A&A, 288, 903 (Paper I)
Cesaroni, R., Olmi, L., Walmsley, C. M., Churchwell, E., & Hofner, P. 1994b, ApJ, 435, L137
Cesaroni, R., Hofner, P., Walmsley, C. M., & Churchwell, E. 1998, A&A, 331, 709 (Paper II)
Cesaroni, R., Galli, D., Lodato, G., Walmsley, C. M., & Zhang, Q. 2007, in Protostars and Planets V, ed. B. Reipurth, D. Jewitt, & K. Keil (Tucson: Univ. of Arizona Press), 197
Churchwell, E., Walmsley, C. M., & Cesaroni, R. 1990, A&AS, 83, 119
Franco, J., Tenorio-Tagle, G., & Bodenheimer, P. 1990, ApJ, 349, 126
Furuya, R. S., Cesaroni, R., Takahashi, S., et al. 2005, ApJ, 624, 827
Fontani, F., Cesaroni, R., Caselli, P., & Olmi, L. 2002, A&A, 389, 603
Gibb, A. G., Wyrowski, F., & Mundy, L. G. 2004, ApJ, 616, 301
Girart, J. M., Beltrán, M. T., Zhang, Q., Rao, R., & Estalella, R. 2009, Science, 324, 1408
Hoare, M. G., Kurtz, S., Lizano, S., Keto, E., & Hofner, P. 2007, in Protostars and Planets V, ed. B. Reipurth, D. Jewitt, & K. Keil (Tucson: Univ. of Arizona Press), 181
Keto, E. H. 2002, ApJ, 580, 980
Keto, E. H. 2003, ApJ, 599, 1196
Keto, E. H. 2007, ApJ, 666, 976
Keto, E. H., & Wood, K. 2006, ApJ, 637, 850
Krumholz, M. R., Klein, R. I., McKee, C. F., Offner, S. S. R., & Cunningham, A. J. 2009, Science, 323, 754

Kurtz, S., Cesaroni, R., Churchwell, E., Hofner, P., & Walmsley, C. M. 2000, in Protostars and Planets IV, ed. V. Mannings, A. Boss, & S. Russel (Tucson: Univ. of Arizona Press), 299
López-Sepulcre, A., Codella, C., Cesaroni, R., Marcelino, N., & Walmsley, C. M. 2009, A&A, 499, 811
Martins, F., Schaerer, D., & Hillier, D. J. 2002, A&A, 382, 999
Maxia, C., Testi, L., Cesaroni, R., & Walmsley, C. M. 2001, A&A, 371, 287
Myers, P. C., Mardones, D., Tafalla, M., Williams, J. P., & Wilner, D. J. 1996, ApJ, 465, L133
Olmi, L., Cesaroni, R., & Walmsley, C. M. 1996a, A&A, 307, 599
Olmi, L., Cesaroni, R., Neri, R., & Walmsley, C. M. 1996b, A&A, 315, 565
Osorio, M., Anglada, G., Lizano, S., & D'Alessio, P. 2009, ApJ, 694, 29
Panagia, N. 1973, AJ, 78, 929
Panagia, N., & Felli, M. 1975, A&A, 39, 1
Pandian, J. D., Momjian, E., & Goldsmith, P. F. 2008, A&A, 486, 191
Poynter, R. L., & Kakar, R. K. 1975, ApJS, 29, 87
Sewilo, M., Watson, C., Araya, E., et al. 2004, ApJ, 154, 553
Ungerechts, H., Walmsley, C. M., & Winnewisser, G. 1986, A&A, 157, 207
Van Dishoeck, E. F., Blake, G. A., Draine, B. T., & Lunine, J. I. 1993, Protostars and Planets III, ed. E. H. Levy, & J. I. Lunine (Tucson: Univ. of Arizona Press), 163
Wilner, D. J., De Pree, C. G., Welch, W. J., & Goss, W. M. 2001, ApJ, 550, L81
Wood, D. O. S., & Churchwell, E. 1989, ApJ, 69, 831
Wu, Y., Wei, Y., & Zhao, M. 2004, A&A, 426, 503
Yorke, H. W. 1985, in Birth and Infancy of Stars, 645
Zhang, Q. 2005, in Massive Star Birth: a Crossroads of Astrophysics, ed. R. Cesaroni, M. Felli, E. Churchwell, & M. Walmsley (Cambridge University Press), IAU Symp., 227, 135